coatings

MDPI

Article

Abrasion Resistance of Superhydrophobic Coatings on Aluminum Using PDMS/SiO_2

Divine Sebastian [1], Chun-Wei Yao [1,*] and Ian Lian [2]

[1] Department of Mechanical Engineering, Lamar University, Beaumont, TX 77710, USA; dsebastian1@lamar.edu
[2] Department of Biology, Lamar University, Beaumont, TX 77710, USA; ilian@lamar.edu
* Correspondence: cyao@lamar.edu; Tel.: +1-409-880-7008

Received: 28 October 2018; Accepted: 20 November 2018; Published: 21 November 2018

Abstract: Superhydrophobic coatings have shown tremendous improvement in the usability of metals such as aluminum. These coatings are capable of adding attractive features such as self-cleaning, anti-corrosion, and anti-biofouling to the array of diverse features that aluminum possesses, including lightweight and high ductility. For superhydrophobic surfaces, having considerable abrasion resistance is as important as achieving a high contact angle. In this work, two types of coatings have been prepared, each composed of functionalized silica nanoparticles along with polydimethylsiloxane (PDMS) dispersed in ethanol, and their superhydrophobicity and abrasion characteristics have been investigated. The same silica nanoparticles are present in each coating, but each has a different proportion of the PDMS base to its curing agent. The surface morphology of the coatings was studied with the aid of a scanning electron microscope (SEM) and an atomic force microscope (AFM). The surface chemical composition was characterized using an energy dispersive X-ray spectroscope (EDX). The prepared coatings were analyzed for their degree of superhydrophobicity, abrasion resistance and adhesion characteristics. In addition, atomic force microscopy was used to understand the adhesion characteristics of the coatings.

Keywords: superhydrophobic coating; aluminum; silica nanocomposite; PDMS

1. Introduction

Artificial superhydrophobic coatings for aluminum have received tremendous attention in the recent past. It is mainly due to their practical applications such as applications in the aerospace industry owing to the capability of such coatings to provide numerous functionalities. These functionalities include self-cleaning [1], anti-icing [2], anti-corrosion [3], and anti-biofouling [4] in addition to the native features of aluminum metal such as lightweight and commendable ductility. A wide variety of fabrication techniques are available for the creation of such coatings, which includes but is not limited to the template method [5], chemical etching [6], electro-spinning [7], chemical vapor deposition [8], self-assembled monolayers [9], and nanocomposites [10–12]. The two governing factors for developing a superhydrophobic coating are its surface chemistry (low surface free energy) and surface morphology (nano/microscale roughness) [13–15]. Many approaches follow a practice of different fabrication stages for the alteration of surface morphology and surface chemistry in a sequential manner [16]. The advantage of using nanoparticle-based composites is that the composite coating offers the required low surface free energy and surface morphology alteration by the proper tuning of its constituents and controlling parameters such as mixing time and application conditions.

Silica nanoparticles are among the most widely used nanoparticles for superhydrophobic coatings, owing to their high degree of reactivity with organic groups, tunable particle size, and comparatively lower cost [17]. Many studies have used different types of fluorinated silanes with silica nanoparticles

in order to achieve low surface free energy [18]. However, functionalized silica nanoparticles have generally exhibited critical issues related to adherence and mechanical durability.

Therefore, Polydimethylsiloxane (PDMS) is often added as a binder or functionalizing agent in the silica nanoparticle coatings since it is hydrophobic in nature and has commendable durability, abrasion resistance, and adherence [19,20]. The most widely used types of PDMS network in research are PDMS 10:1 (base/agent ratio) and 5:1 if enhanced mechanical properties are desired [21–23].

There are various factors that determine the resulting coating's quality and durability; these factors include but are not limited to the proportion of various constituents within the solution [24], temperature [25] and curing time [26]. In this work, functionalized silica nanoparticles were used along with PDMS to create superhydrophobic nanocomposite coatings that were later applied to aluminum substrates. Two base/agent ratios of PDMS were used for developing nanocomposite solutions as it was inferred from past studies that the mechanical properties such as stiffness of the polymer network vary with respect to the proportion between polymer base and curing agent [21–23]. In this study, an attempt is made to see whether such shift in polymer network's mechanical properties with respect to the proportion between polymer base and curing agent can be replicated in case of nanocomposites where these polymers are used. As mechanical durability is an important factor in determining the quality of superhydrophobic coatings [27], various abrasion resistance tests were performed on both coatings. The resistance to abrasion while maintaining a non-wetting state can be seen from the results of abrasion tests. Furthermore, the results of atomic force microscope (AFM) characterization for adhesion properties and contact angle measurements were discussed.

2. Materials and Methods

2024-T3 aluminum alloy plates of 5 cm × 5 cm × 0.5 mm were used as the substrates. Chemicals used were anhydrous ethanol (Sigma Aldrich, St. Louis, MO, USA), isopropyl alcohol (Sigma Aldrich, St. Louis, MO, USA), acetone (Sigma Aldrich, St. Louis, MO, USA), polydimethylsiloxane elastomer kit (Sylgard 184) (Dow Corning, Midland, MI, USA). Silane-modified hydrophobic SiO_2 nanoparticles (RX-50) with average diameter of 55 nm (±15 nm) were obtained from Evonik (Piscataway, NJ, USA). All experiments were conducted at room temperature of 25 °C.

The flat aluminum substrates were initially cleaned using ultrasonication in acetone for 15 min followed by rinsing with isopropyl alcohol, ethanol, and deionized water to clean off surface contaminants and grease and finally dried in air. After performing initial cleaning, 1.5 g of silica nanoparticle was added to 10 g of ethanol and then the suspension of nanoparticles in ethanol was dispersed by ultrasonic stirring for 30 min followed by mechanical stirring for 30 min. This step enables the proper dispersion of nanoparticles without aggregation. After the initial stirring, 1 g of PDMS was added into the solution followed by mechanical stirring for 30 min and then 0.1 g of curing agent for coating Solution A and 0.2 g of curing agent for coating Solution B were added in separate preparation schedules. The solution was further mechanically stirred for another 30 min. The prepared coating was deposited on the cleaned aluminum substrates by spin coating at a speed of 500 rpm for 15 s. The coating was then oven-cured at 165 °C for 5 min followed by air cooling in a fume hood.

The morphologies and chemical compositions of the superhydrophobic aluminum surfaces were assessed using a scanning electron microscope (SEM, Hitachi S-3400N, Hitachi High Technologies, Tokyo, Japan) equipped with energy-dispersive X-ray spectroscopy, and an atomic force microscope (AFM, Park NX10, Park System Co., Suwon, Korea). The water contact angles were measured using a drop shape analyzer (DSA25E, Krüss, Hamburg, Germany). Water droplets (10 µL) were dropped onto the surfaces under ambient temperature and atmosphere. A manually operated linear mechanical abrasion test was performed using 240-grit sandpaper with 7.75 kPa normal pressure. An automated linear mechanical abrasion was performed with a linear abrader (Taber Industries, New York, NY, USA) using CS-10F Calibrase abradant under 29.9 kPa applied pressure.

3. Results and discussion

3.1. Effect of Nanoparticles Concentration on Wettability

As explained in the previous section, two types of nanocomposite solutions were prepared, designated as Coatings A and B, where the weight proportion of ethanol and nanoparticles remained the same with the distinction being the ratio between the polymer base and the curing agent for polydimethylsiloxane. Coating A was prepared using a ratio of 10:1, whereas for Coating B, the ratio between the polymer base and the curing agent was 5:1. The variation in hydrophobicity of the coating with respect to the varying weight proportions of silica nanoparticles in terms of static contact angle and roll-off angle is shown in Figure 1. It can be observed that even for a lower weight proportion of 0.2 g nanoparticle in 10 g solvent, the resulting static water contact angle was close to 120°, which increased continuously up to 1.5 g where the static contact angle averaged over 160°. A further increase in the quantity of nanoparticles resulted in a decline of the static contact angle. The lowest roll-off angle was also observed when having 1.5 g nanoparticles; thus, 1.5 g nanoparticles in 10 g solvent were considered to be the standardized amount of nanoparticles for both solutions. It should be noted that the data used in Figure 1 is with the ratio of 10:1 for the PDMS, and a similar trend was observed in the case of the ratio of 5:1 for PDMS. The variation in degree of hydrophobicity can be related to the average surface roughness of coatings as shown in Table 1 in which the highest roughness was obtained when having 1.5 g nanoparticles.

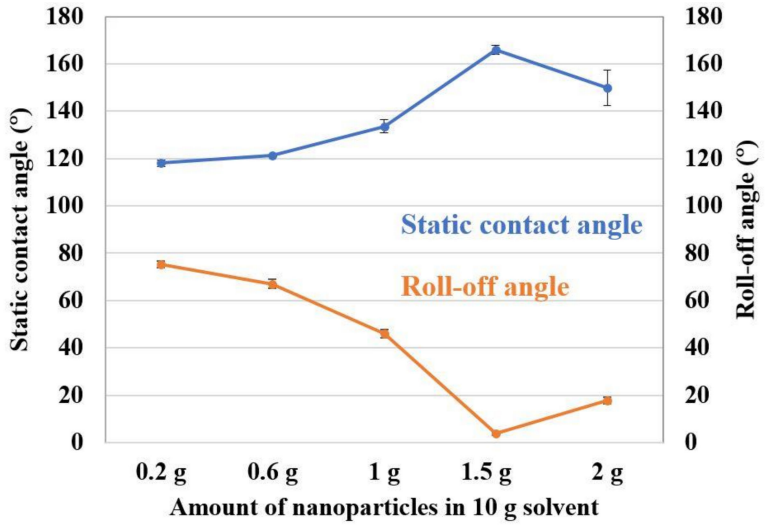

Figure 1. Static Contact angle and roll-off angle as a function of varying nanoparticle composition.

Table 1. Average surface roughness values for coating as a function of varying nanoparticle composition.

Amount of Nanoparticles in 10 g Solvent (g)	Average Roughness (nm)
0.2	94 ± 2
0.6	171 ± 3
1	266 ± 3
1.5	359 ± 4
2	321 ± 4

3.2. Surface Morphology and Chemical Composition

Figure 2 shows the SEM images of surfaces with Coatings A and B at two different magnifications. The dense structures observed in both coatings contribute to their high roughness, and it can be observed that the visual appearance of both coatings is considerably similar; this similarity is logical as the same nanoparticles with identical weight proportions were used. The chemical composition of the developed coatings was verified with the aid of an energy dispersive X-ray spectroscope (EDX).

Figure 3 shows the EDX spectrum for coating A. EDX data indicate without doubt the presence of Si and O, which suggests the proper dispersion of silica nanoparticles throughout the coating, and the presence of C along with O accounts for the functionalizing chemicals used. The EDX spectrum for coating B was identical to that of coating A, which can be explained by the use of the same chemicals and fabrication sequence with a slight variation in only one of the constituent chemicals. Figure 4 shows the three-dimensional AFM images of both coatings. The average roughness for Coatings A and B was found to be 359 ± 4 nm and 358 ± 4 nm, respectively.

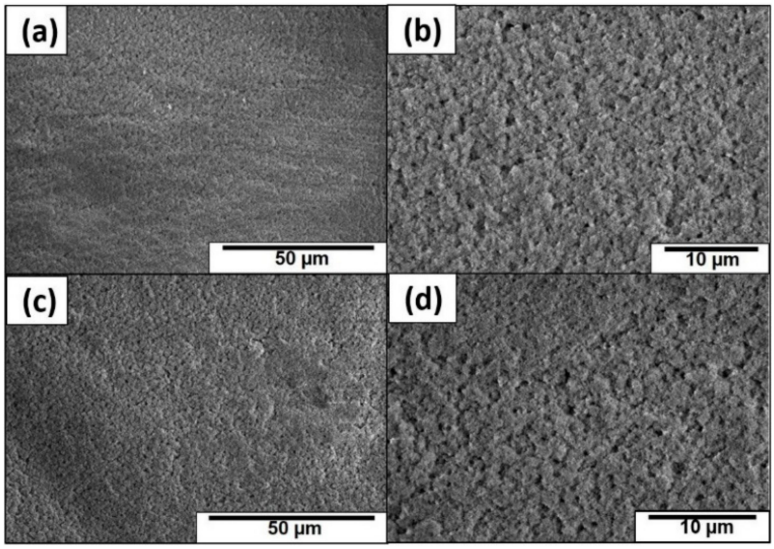

Figure 2. Scanning electron microscope (SEM) images of the superhydrophobic aluminum surfaces with the Coating A (**a**,**b**) and Coating B (**c**,**d**).

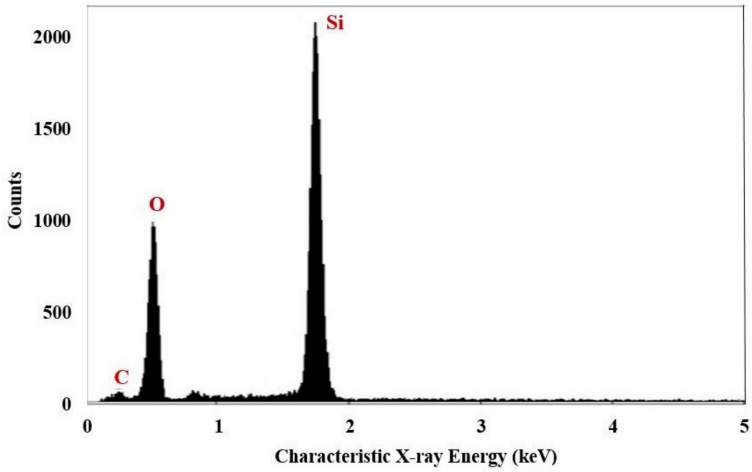

Figure 3. Energy dispersive X-ray spectroscope (EDX) spectrum analysis of superhydrophobic aluminum surface with Coating A.

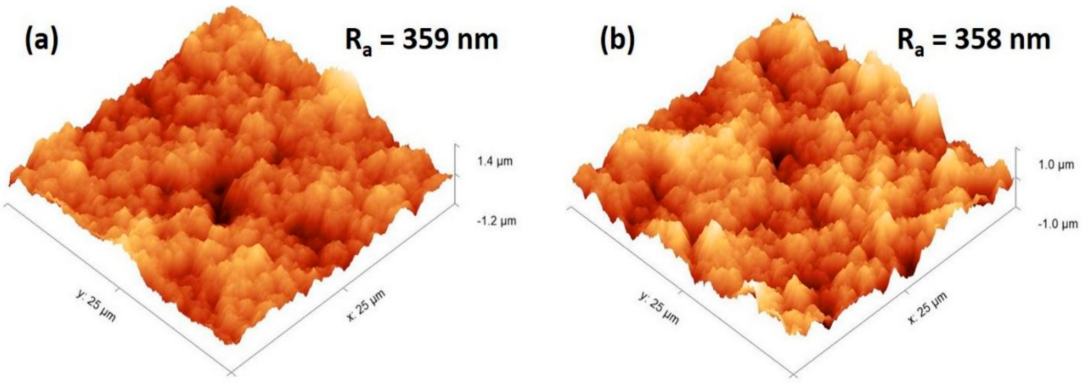

Figure 4. 3-Dimensional atomic force microscope (AFM) image of the (**a**) superhydrophobic aluminum surface with Coating A and (**b**) superhydrophobic aluminum surface with Coating B.

3.3. Wetting Properties of Coatings

Static contact angles and roll-off angles were measured for Coatings A and B to study their wetting behavior. Average static contact angle for Coating A was found to be 166° ± 0.9° and that of Coating B was found to be 162° ± 0.6°. Figure 5 shows the representational images corresponding to static water contact angles for Coatings A and B. According to static water contact angles, coating A is slightly superior over coating B, which is reiterated by the average roll-off angle of 3° for Coating A and 4° for Coating B.

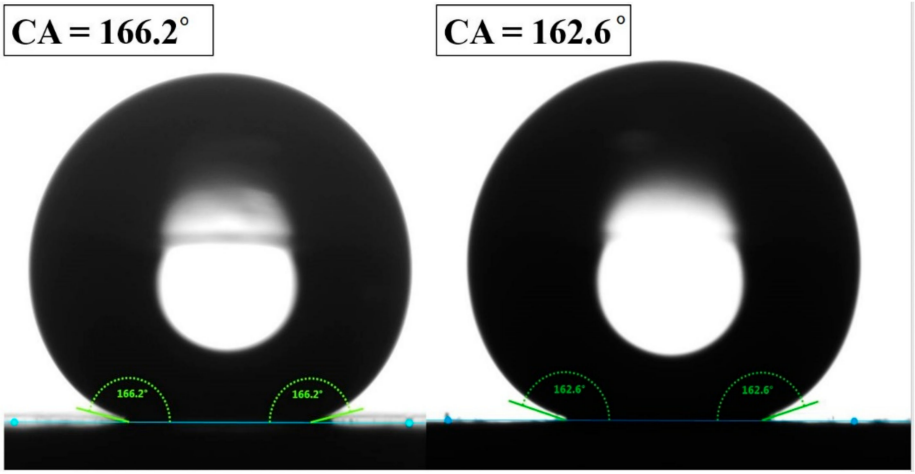

Figure 5. Static water contact angles obtained on (**a**) superhydrophobic aluminum surface with the Coating A and (**b**) superhydrophobic aluminum surface with the Coating B.

3.4. Adhesion Characteristics of the Coatings

Table 2 lists the adhesion force, adhesion energy, and average roughness as characterized by AFM. The adhesion forces of both coatings are considerably close to each other, which essentially indicates that the adhesive characteristics of the developed coatings do not show a high deviation from each other, with Coating A having the upper hand in terms of adhesion force. A similar trend in the case of adhesion energy for Coatings A and B reiterates the observations made for adhesion force for both coatings. The average roughness values are close to each other and can be accounted for by the identical nanoparticles and fabrication sequence. The slight superiority of Coating A in terms of adhesive characteristics could be because of the better binding effect of the PDMS network in the case of Coating A.

Table 2. Average roughness, adhesion force and adhesion energy of the superhydrophobic aluminum surfaces.

Surface Characteristics	Average Roughness R_a (nm)	Adhesion Force (nN)	Adhesion Energy (fJ)
Coating A	359 ± 4	6.29 ± 0.57	0.083 ± 0.010
Coating B	358 ± 4	5.43 ± 0.66	0.064 ± 0.010

3.5. Abrasion Resistance of the Coating

Mechanical stability and durability of the superhydrophobic coating are important in view of its usage in practical applications. Abrasion resistance of the coating provides reliable information about its mechanical stability. In this work, the abrasion resistance of coatings was analyzed using two approaches. In the first approach, the coating was dragged against a 240-grit sandpaper with 7.75 kPa normal pressure. The sandpaper, which acts as the abrading surface used in this work, is considerably rougher than the sandpapers used in similar tests that are listed in Table 3 [24,28–36]; hence, it provides a more severe abrading action. The specimen, under exerted pressure, was moved in 20 cm cycles, rotating the specimen by 90° at the halfway point of each cycle to introduce even abrasions on the coating's surface. Figure 6 shows the variation in static contact angles for coating A as well as for Coating B, with reference to the number of abrasion cycles. Both coatings showed the highest decrease in a single cycle of abrasion, in the case of the first abrasion cycle. Coating A exhibited a decrease in contact angle by 12° for the first abrasion cycle, whereas the corresponding value for Coating B was 15°. This drastic decrease in the first cycle can be explained by the damage to fine, delicate nanocomposite structures that extend from the dense network. After the first cycle of abrasion, an irregular increase in the contact angles was observed for both coatings between arbitrary abrasion cycles. The general trend observed for Coating B was a continuous decrease in contact angles as the number of abrasion cycles increased, whereas for Coating A, the contact angles fluctuated within 145° and 155° for up to 20 abrasion cycles. Coating B maintained contact angles over 140° for up to 18 abrasion cycles, and a higher rate of decrease was observed afterward. Both coatings maintained contact angles over 115° even after 50 abrasion cycles. Figure 7 shows the variation in roll-off angles for coating A as well as for Coating B, with reference to the number of abrasion cycles. There is a continuous increase in roll-off angles for both coatings as the number of abrasion cycles increases; this increase substantiates the damage behavior observed from the static contact angles. After 30 cycles of abrasion, roll-off angles of both coatings stabilized with Coating A specifically around 75° and Coating B over 80°. Figure 8 shows the SEM images of Coating A at different magnifications and highlights the morphological variation between the initial and final stages of the abrasion test. From Figure 8a,b, it is observed that the coating is fairly uniform, and the silica nanocomposite is evenly dispersed. But after 50 cycles of abrasion, the aluminum substrate is slightly exposed, and the coating is ruptured at multiple locations, as seen in Figure 8c,d as a result of sandpaper abrasion. Figure 9 shows the corresponding SEM images for Coating B. From Figure 9a,b, it can be seen that the coating is fairly uniform, and the silica nanocomposite is evenly dispersed and considerably identical to Coating A at the initial stage. But after 50 cycles of abrasion, the aluminum substrate is even more exposed, as seen in Figure 9c,d, as a result of sandpaper abrasion, and damage to the coating is severe. The results reveal that the susceptibility of both coatings to damage, when exposed to identical abrading conditions, falls in an agreeable range.

Table 3. Summary of published works on the mechanical durability of silica nanoparticle based superhydrophobic coatings using Sandpaper abrasion tests and Taber linear abrasion tests. The current study included at the end of the table for the purpose of comparison.

Nanoparticles	Substrate	Nanoparticle Functionalization	Durability Test	Force Applied	Number of Abrasion Cycles	Distance of One Cycle	Sandpaper Grit Number/Abrader Grade	Ref.
Silica	Wood	Vinyl triethoxysilane	Sandpaper	0–12 kPa 100 g	NA	150–1050 mm	3000 mesh	[28]
Silica (R972, 16 nm)	Glass	1H,1H,2H,2H-Perfluorooctyltriethoxysilane	Sandpaper	50 g	9	200 mm	150	[29]
Hydrophobic fumed Silica nanoparticles (Aerosil R972)	Aluminum	Dimethyl dichlorosilane	Sandpaper	10 kPa	Not given	Not given	Not mentioned	[30]
Silica	Polyester	TEOS	Sandpaper	5 kPa	200	400 mm	2000 mesh	[31]
Fluorinated silica nanoparticles, titania nanoparticles	NA	Fluorinated alkylsilane	Sandpaper	10 kPa, 20 kPa	10	Not given	Not mentioned	[32]
Silica nanoparticles (40 nm)	Polyester fabrics	PFDTS, PFOTS, TEOS	Sandpaper	10 kPa	100	Not given	Not mentioned	[33]
Silica nanoparticles	Polyester	TEOS, MTES, OTES, DDTES, HDTES, ODTES	Sandpaper, A4 paper	5 kPa	200	400 mm	2000 mesh	[34]
Silica nanoparticles (10-20 nm)	Wood	1H,1H,2H,2H-perfluorodecyltriethoxysilane	Sandpaper	5 kPa	10	250 mm	1500 mesh	[35]
Silica nanoparticles	Wood	HDTMS, PDMS	Sandpaper	12.5 kPa	10	300 mm	1500 mesh	[36]
Silica nanoparticles (RX-50) Aerosil, Evonik	Aluminum	Hexamethyldisilazane (HMDS)	Sandpaper & Taber linear abrader	100 g	50	200 mm	240	Current work
Hydrophobic fumed silica nanoparticles	Aluminum	Pre-functionalized	Taber linear abrader (Model 5750)	20 kPa	30	100 mm	CS-10F Callibrase	[24]
Hydrophobic fumed silica nanoparticles	Silicon	Hexamethyldisilazane (HMDS)	Taber linear abrader	2.1 kPa	20	80 mm	Plastic disk	[37]
Hydrophobic fumed silica nanoparticles	Aluminum	Hexamethyldisilazane (HMDS)	Taber linear abrader (Model 5750)	17.5 kPa	35	50 mm	CS-8 Calibrase	[38]
Silica nanoparticles (RX-50) Aerosil, Evonik	Aluminum	Hexamethyldisilazane (HMDS)	Taber linear abrader	29.9 kPa	30	Full length of sample	CS-10F Callibrase	Current work

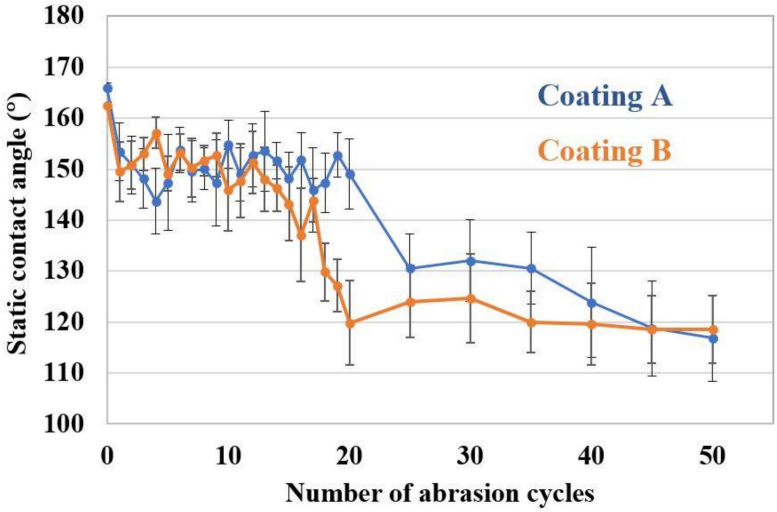

Figure 6. Static contact angles after abrasion against a 240-grit sandpaper with 7.75 kPa normal load.

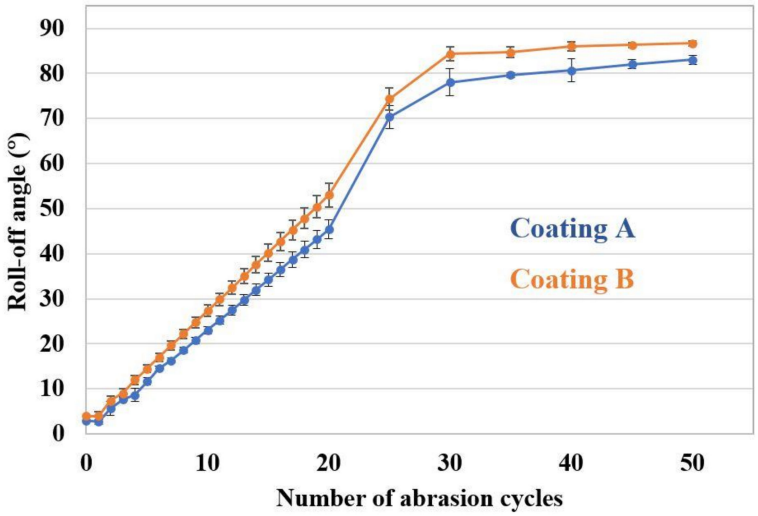

Figure 7. Roll-off angles after abrasion against a 240-grit sandpaper with 7.75 kPa normal load.

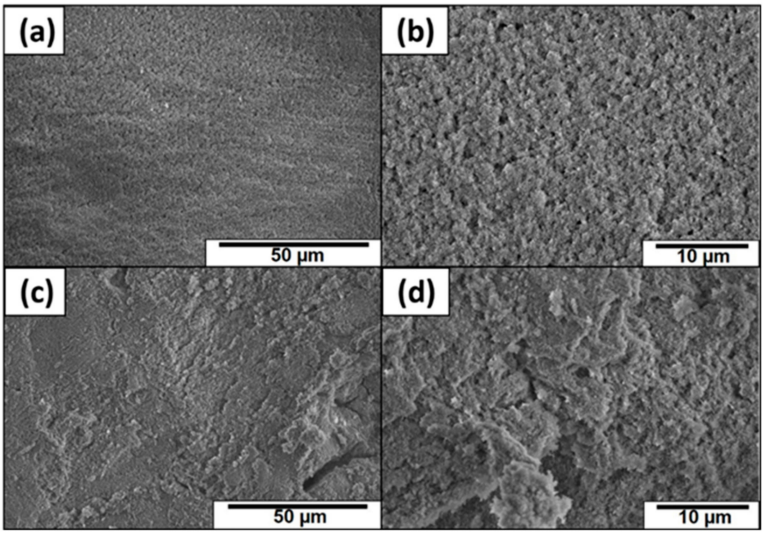

Figure 8. SEM images of the superhydrophobic aluminum surfaces with the Coating A: (**a**,**b**) surface layer before abrasion at different magnifications; (**c**,**d**) surface layer after 50 cycles of abrasion at different magnifications.

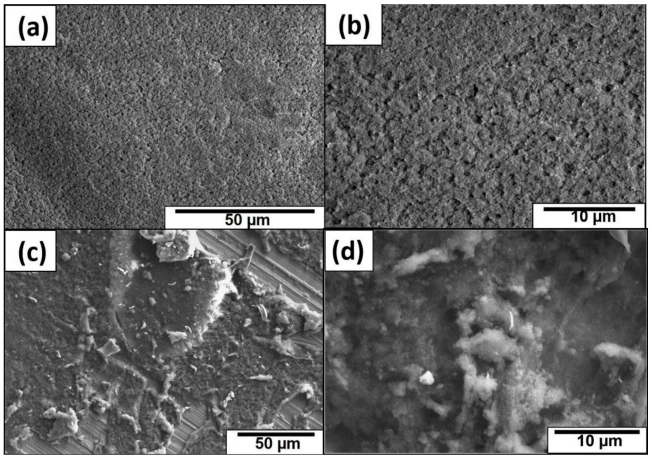

Figure 9. SEM images of the superhydrophobic aluminum surfaces with the Coating B: (**a**,**b**) surface layer before abrasion at different magnifications; (**c**,**d**) surface layer after 50 cycles of abrasion at different magnifications.

Table 3 offers a list of works from the literature where linear abraders were used for the study of abrasion resistance characteristics of nanocomposite coatings using silica nanoparticles [24,37,38]. In the second approach, the abrasion test was carried out using a Taber linear abrader under a constant load of 29.9 kPa applied pressure. The pressure used in this work for the linear abrasion test is significantly higher than some values reported in the literature involving similar tests as shown in Table 3 [24,37,38]. The stroke speed was maintained at a constant value of 15 cycles/min. Changes in static contact angles and roll-off angles were measured after every set of two linear abrasion cycles. The abradant used for the test was a cylindrically shaped material known as CS-10F Calibrase (1.26 cm in diameter) that produces mild abrading action. Figure 10 shows the variation in static contact angles for Coating A as well as for Coating B with reference to the number of abrasion cycles. Both coatings exhibited a continuous decrease in the contact angle with only a very few cycles where there was a slight increase in the contact angle. After 30 abrasion cycles under a constant load of 29.9 kPa, Coating A reached the lowest contact angle value of 108°, and coating B stabilized in terms of the contact angle around 104°. Figure 11 shows the variation in roll-off angles for Coating A as well as for Coating B with reference to the number of abrasion cycles. There is a continuous increase in roll-off angles for both coatings, a trend observed in previous abrasion tests as well. After 30 cycles of abrasion, roll-off angles of both coatings stabilized, with Coating A specifically around 70° and Coating B over 76°. Figure 11 shows the SEM images of surfaces with Coating A at different magnifications that highlight the morphological variation between the initial and final stages of the abrasion test. From Figure 12 a,b, it can be seen that the coating is fairly uniform, and the silica nanocomposite is evenly dispersed. But after 30 cycles of abrasion, the aluminum substrate is exposed, and the damage to the coating is easily observed, as seen in Figure 12 c,d, as a result of sandpaper abrasion. Figure 13 shows the corresponding SEM images for coating B. From Figure 13 a,b, it can be seen that the coating is fairly uniform, and the silica nanocomposite is evenly dispersed and practically identical to coating A at the initial stage. But after 30 cycles of abrasion, the aluminum substrate is exposed even more as a result of sandpaper abrasion, as seen in Figure 13 c,d, and the damage to the coating is severe. The results of the Taber abrasion test clearly agree with the same from the sandpaper abrasion test. Furthermore, these results could be related to the adhesion characteristics observed in the previous section as well. Based on the SEM images and abrasion test results, Coating A is slightly superior over Coating B and it agrees with the observations made for adhesion characteristics where Coating A exhibited a slight dominance. The static contact angle measurements show that Coating A has a slight advantage over Coating B after 30 cycles of abrasions, though both coatings were fairly stable up to 15 cycles of abrasion and maintained appreciable hydrophobic behavior. Additionally, based on the SEM

images and observing the exposed area, the damage to Coating B is comparatively severe after the rupture of the coating.

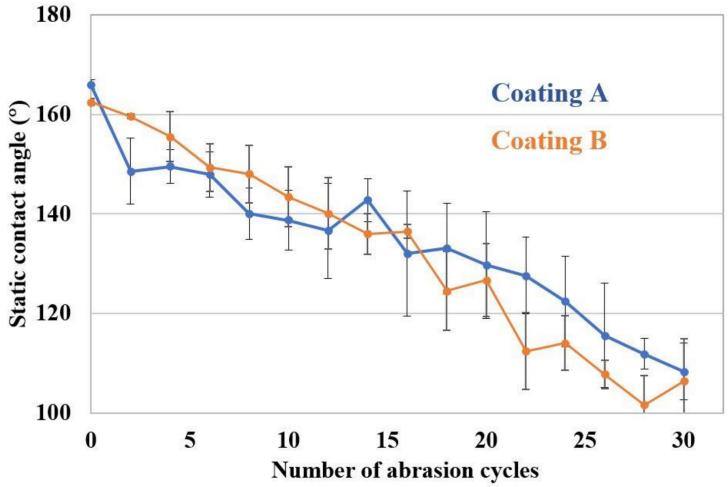

Figure 10. Static contact angles after Taber abrasion test against 29.9 kPa normal load.

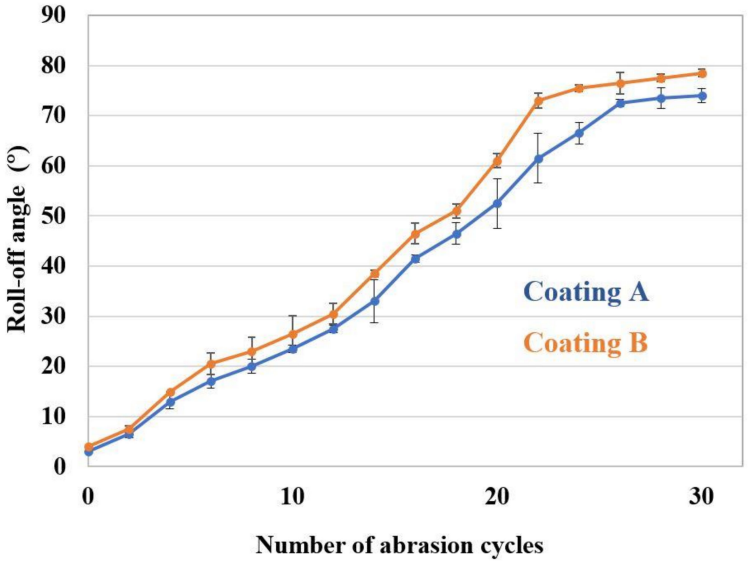

Figure 11. Roll-off angles after the Taber abrasion test against 29.9 kPa normal load.

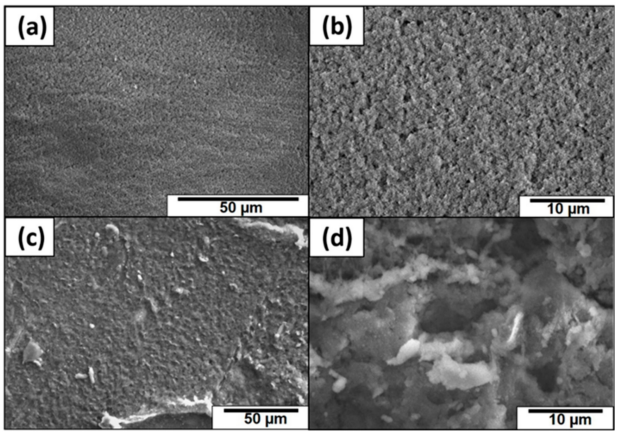

Figure 12. SEM images of the superhydrophobic aluminum surfaces with the Coating A: (**a**,**b**) surface layer before Taber abrasion test at different magnifications; (**c**,**d**) surface layer after 30 cycles of Taber abrasion test at different magnifications.

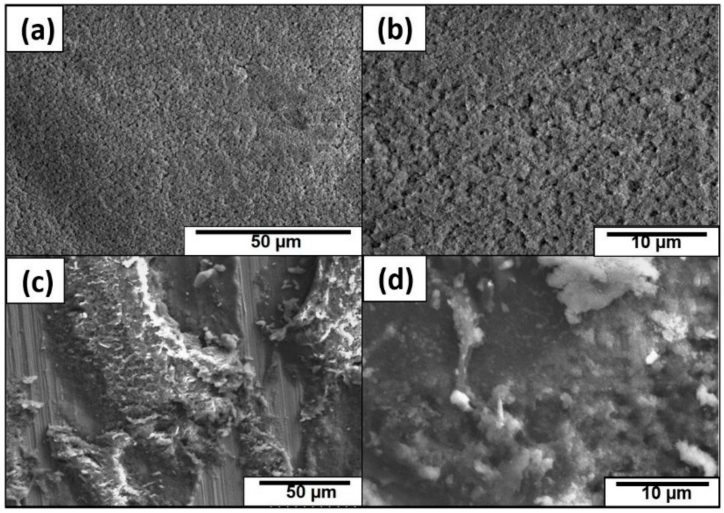

Figure 13. SEM images of the superhydrophobic aluminum surfaces with the Coating B: (**a**,**b**) surface layer before Taber abrasion test at different magnifications; (**c**,**d**) surface layer after 30 cycles of Taber abrasion test at different magnifications.

4. Conclusions

In this work, two types of coatings were developed and featured excellent superhydrophobicity and considerable mechanical durability. The static water contact angles for both coatings were over 160° for both coatings. AFM studies showed that the average roughness values and the quantified adhesion properties for both coatings are close to each other. The abrasion resistance of superhydrophobic coatings for aluminum was investigated in detail. Only relatively small changes in the wettability of both coatings were observed after sandpaper abrasion. During the more severe linear abrasion test, both coatings maintained their superhydrophobic behavior up to a considerable number of abrasion cycles and started to show a slight reduction after each cycle. Moreover, the difference of robustness between these two coatings is minor. These coatings for aluminum metal can be used in applications where superhydrophobicity is a significant requirement.

Author Contributions: Formal Analysis, D.S.; Supervision, C.-W.Y.; Writing–Original Draft Preparation, D.S. and C.-W.Y.; Writing–Review & Editing, C.-W.Y. and I.L.

Funding: This research was funded by 2018 Research Enhancement Grant (REG) Award, Lamar University.

Acknowledgments: This work was supported by Center for Advances in Port Management (CAPM) of Lamar University, and Center for Advances in Water and Air Quality (CAWAQ) of Lamar University. The authors would like to thank Carrie Martin for her assistance during SEM characterization. The authors appreciate the Center for Innovation, Commercialization and Entrepreneurship (CICE) at Lamar University for providing lab space.

Conflicts of Interest: The authors declare no conflict of interest.

References

1. Wang, Z.; Li, Q.; She, Z.; Chen, F.; Li, L. Low-cost and large-scale fabrication method for an environmentally-friendly superhydrophobic coating on magnesium alloy. *J. Mater. Chem.* **2012**, *22*, 4097–4105. [CrossRef]
2. Jung, S.; Dorrestijn, M.; Raps, D.; Das, A.; Megaridis, C.M.; Poulikakos, D. Are superhydrophobic surfaces best for icephobicity? *Langmuir* **2011**, *27*, 3059–3066. [CrossRef] [PubMed]
3. Yao, C.W.; Sebastian, D.; Lian, I.; Günaydın-Şen, Ö.; Clarke, R.; Clayton, K.; Chen, C.; Kharel, K.; Chen, Y.; Li, Q. Corrosion resistance and durability of superhydrophobic copper surface in corrosive NaCl aqueous solution. *Coatings* **2018**, *8*, 70. [CrossRef]
4. Yang, W.; Li, J.; Zhou, P.; Zhu, L.; Tang, H. Superhydrophobic copper coating: switchable wettability, on-demand oil-water separation, and antifouling. *Chem. Eng. J.* **2017**, *327*, 849–854. [CrossRef]

5. Tao, C.; Yan, H.; Yuan, X.; Yao, C.; Yin, Q.; Zhu, J.; Ni, W.; Yan, L.; Zhang, L. Synthesis of shape-controlled hollow silica nanostructures with a simple soft-templating method and their application as superhydrophobic antireflective coatings with ultralow refractive indices. *Colloids Surf. A* **2016**, *501*, 17–23. [CrossRef]
6. Qian, B.; Shen, Z. Fabrication of superhydrophobic surfaces by dislocation-selective chemical etching on aluminum, copper, and zinc substrates. *Langmuir* **2005**, *21*, 9007–9009. [CrossRef] [PubMed]
7. Bahgat, A.; Mohamed, A.; Abdullah, A.; Almaadeed, M. Superhydrophobic and corrosion behavior of electrospun PVDF-ZnO coating. *ECS Trans.* **2015**, *64*, 57–67. [CrossRef]
8. Yu, J.; Qin, L.; Hao, Y.; Kuang, S.; Bai, X.; Chong, Y.M.; Zhang, W.; Wang, E. Vertically aligned boron nitride nanosheets: Chemical vapor synthesis, ultraviolet light emission, and superhydrophobicity. *ACS Nano* **2010**, *4*, 414–422. [CrossRef] [PubMed]
9. Boinovich, L.B.; Emelyanenko, A.M. The behaviour of fluoro-and hydrocarbon surfactants used for fabrication of superhydrophobic coatings at solid/water interface. *Colloids Surf. A* **2015**, *481*, 167–175. [CrossRef]
10. Qing, Y.; Yang, C.; Hu, C.; Zheng, Y.; Liu, C. A facile method to prepare superhydrophobic fluorinated polysiloxane/ZnO nanocomposite coatings with corrosion resistance. *Appl. Surf. Sci.* **2015**, *326*, 48–54. [CrossRef]
11. Zhang, Z.; Ge, B.; Men, X.; Li, Y. Mechanically durable, superhydrophobic coatings prepared by dual-layer method for anti-corrosion and self-cleaning. *Colloids Surf. A* **2016**, *490*, 182–188. [CrossRef]
12. Schaeffer, D.A.; Polizos, G.; Smith, D.B.; Lee, D.F.; Hunter, S.R.; Datskos, P.G. Optically transparent and environmentally durable superhydrophobic coating based on functionalized SiO_2 nanoparticles. *Nanotechnology* **2015**, *26*, 055602. [CrossRef] [PubMed]
13. She, Z.; Li, Q.; Wang, Z.; Li, L.; Chen, F.; Zhou, J. Novel method for controllable fabrication of a superhydrophobic CuO surface on AZ91D magnesium alloy. *ACS Appl. Mater. Interface* **2012**, *4*, 4348–4356. [CrossRef] [PubMed]
14. Zhu, X.; Zhang, Z.; Xu, X.; Men, X.; Yang, J.; Zhou, X.; Xue, Q. Facile fabrication of a superamphiphobic surface on the copper substrate. *J. Colloid Interface Sci.* **2012**, *367*, 443–449. [CrossRef] [PubMed]
15. Chen, Z.; Hao, L.; Chen, A.; Song, Q.; Chen, C. A rapid one-step process for fabrication of superhydrophobic surface by electrodeposition method. *Electrochim. Acta* **2012**, *59*, 168–171. [CrossRef]
16. Xu, Z.; Miyazaki, K.; Hori, T. Fabrication of polydopamine-coated superhydrophobic fabrics for oil/water separation and self-cleaning. *Appl. Surf. Sci.* **2016**, *370*, 243–251. [CrossRef]
17. Xu, L.; Karunakaran, R.G.; Guo, J.; Yang, S. Transparent, superhydrophobic surfaces from one-step spin coating of hydrophobic nanoparticles. *ACS Appl. Mater. Interface* **2012**, *4*, 1118–1125. [CrossRef] [PubMed]
18. Brassard, J.D.; Sarkar, D.K.; Perron, J. Fluorine based superhydrophobic coatings. *Appl. Sci.* **2012**, *2*, 453–464. [CrossRef]
19. Cao, C.; Ge, M.; Huang, J.; Li, S.; Deng, S.; Zhang, S.; Chen, Z.; Zhang, K.; Al-Deyab, S.; Lai, Y. Robust fluorine-free superhydrophobic PDMS–Ormosil@fabrics for highly effective self-cleaning and efficient oil–water separation. *J. Mater. Chem. A* **2016**, *4*, 12179–12187. [CrossRef]
20. Gao, S.; Dong, X.; Huang, J.; Li, S.; Li, Y.; Chen, Z.; Lai, Y. Rational construction of highly transparent superhydrophobic coatings based on a non-particle, fluorine-free and water-rich system for versatile oil-water separation. *Chem. Eng. J.* **2018**, *333*, 621–629. [CrossRef]
21. Kim, T.K.; Kim, J.K.; Jeong, O.C. Measurement of nonlinear mechanical properties of PDMS elastomer. *Microelectron. Eng.* **2011**, *88*, 1982–1985. [CrossRef]
22. Palchesko, R.N.; Zhang, L.; Sun, Y.; Feinberg, A.W. Development of polydimethylsiloxane substrates with tunable elastic modulus to study cell mechanobiology in muscle and nerve. *PLoS One* **2012**, *7*, e51499. [CrossRef] [PubMed]
23. Lei, K.F.; Lee, K.F.; Lee, M.Y. Development of a flexible PDMS capacitive pressure sensor for plantar pressure measurement. *Microelectron. Eng.* **2012**, *99*, 1–5. [CrossRef]
24. Naderizadeh, S.; Athanassiou, A.; Bayer, I.S. Interfacing superhydrophobic silica nanoparticle films with graphene and thermoplastic polyurethane for wear/abrasion resistance. *J. Colloid Interface Sci.* **2018**, *519*, 285–295. [CrossRef] [PubMed]
25. Becker, O.; Cheng, Y.B.; Varley, R.J.; Simon, G.P. Layered silicate nanocomposites based on various high-functionality epoxy resins: The influence of cure temperature on morphology, mechanical properties, and free volume. *Macromolecules* **2003**, *36*, 1616–1625. [CrossRef]

26. Kornmann, X.; Lindberg, H.; Berglund, L.A. Synthesis of epoxy–clay nanocomposites. Influence of the nature of the curing agent on structure. *Polymer* **2001**, *42*, 4493–4499. [CrossRef]
27. Sebastian, D.; Yao, C.; Lian, I. Mechanical durability of engineered superhydrophobic surfaces for anti-corrosion. *Coatings* **2018**, *8*, 162. [CrossRef]
28. Jia, S.; Liu, M.; Wu, Y.; Luo, S.; Qing, Y.; Chen, H. Facile and scalable preparation of highly wear-resistance superhydrophobic surface on wood substrates using silica nanoparticles modified by VTES. *Appl. Surf. Sci.* **2016**, *386*, 115–124. [CrossRef]
29. Wang, P.; Chen, M.; Han, H.; Fan, X.; Liu, Q.; Wang, J. Transparent and abrasion-resistant superhydrophobic coating with robust self-cleaning function in either air or oil. *J. Mater. Chem. A* **2016**, *4*, 7869–7874. [CrossRef]
30. Zhang, Y.; Ge, D.; Yang, S. Spray-coating of superhydrophobic aluminum alloys with enhanced mechanical robustness. *J. Colloid Interface Sci.* **2014**, *423*, 101–107. [CrossRef] [PubMed]
31. Wu, L.; Zhang, J.; Li, B.; Wang, A. Mechanical- and oil-durable superhydrophobic polyester materials for selective oil absorption and oil/water separation. *J. Colloid Interface Sci.* **2014**, *413*, 112–117. [CrossRef] [PubMed]
32. Chen, K.; Zhou, S.; Wu, L. Facile fabrication of self-repairing superhydrophobic coatings. *Chem. Commun.* **2014**, *50*, 11891–11894. [CrossRef] [PubMed]
33. Yokoi, N.; Manabe, K.; Tenjimbayashi, M.; Shiratori, S. Optically transparent superhydrophobic surfaces with enhanced mechanical abrasion resistance enabled by mesh structure. *ACS Appl. Mater. Interfaces* **2015**, *7*, 4809–4816. [CrossRef] [PubMed]
34. Wu, L.; Zhang, J.; Li, B.; Wang, A. Mimic nature, beyond nature: facile synthesis of durable superhydrophobic textiles using organosilanes. *J. Mater. Chem. B* **2013**, *1*, 4756–4763. [CrossRef]
35. Tu, K.; Wang, X.; Kong, L.; Chang, H.; Liu, J. Fabrication of robust, damage-tolerant superhydrophobic coatings on naturally micro-grooved wood surfaces. *RSC Adv.* **2016**, *6*, 701–707. [CrossRef]
36. Chang, H.; Tu, K.; Wang, X.; Liu, J. Fabrication of mechanically durable superhydrophobic wood surfaces using polydimethylsiloxane and silica nanoparticles. *RSC Adv.* **2015**, *5*, 30647–30653. [CrossRef]
37. Milionis, A.; Ruffilli, R.; Bayer, I. Superhydrophobic nanocomposites from biodegradable thermoplastic starch composites (mater-bi®), hydrophobic nano-silica and lycopodium spores. *RSC Adv.* **2014**, *4*, 34395–34404. [CrossRef]
38. Masood, M.T.; Heredia-Guerrero, J.A.; Ceseracciu, L.; Palazon, F.; Athanassiou, A.; Bayer, I.S. Superhydrophobic high impact polystyrene (HIPS) nanocomposites with wear abrasion resistance. *Chem. Eng. J.* **2017**, *322*, 10–21. [CrossRef]